Electronic Structure

Improving the precision of work-function calculations within plane-wave density functional theory

To cite this article before publication: Yiyuan Wang *et al* 2024 *Electron. Struct.* in press https://doi.org/10.1088/2516-1075/ad72c2

Improving the precision of work-function calculations within plane-wave density functional theory

Yiyuan Wang[1,*], **Sari J Laihonen**[2], **Mikael Unge**[3] **and Arash A Mostofi**[1,*]

[1] Departments of Materials and Physics, and the Thomas Young Centre for Theory and Simulation of Materials, Imperial College London, Exhibition Road, London SW7 2AZ, UK

[2] Hitachi Energy Research, Forskargränd 7, 721 78 Västerås, Sweden

[3] NKT HV Cables AB, Technology Consulting, 722 26 Västerås, Sweden

*Authors to whom any correspondence should be addressed.

E-mail: amyyiyuan627@gmail.com, a.mostofi@imperial.ac.uk

Abstract. Work function is a fundamental property of metals and is related to many surface-related phenomena of metals. Theoretically, it can be calculated with a metal slab supercell in density functional theory (DFT) calculations. In this paper, we discuss how the commensurability of atomic structure with the underlying fast Fourier transform (FFT) grid affects the accuracy of work function obtained from plane-wave pseudopotential DFT calculations. We show that the macroscopic average potential, which is an important property in work function calculations under the 'bulk reference' method, is more numerically stable when it is calculated with commensurate FFT grids than with incommensurate FFT grids. Due to the stability of the macroscopic average potential, work function calculated with commensurate FFT grids shows better convergence with respect to basis set size, vacuum length and slab thickness of a slab supercell. After we control the FFT grid commensurability issue in our work function calculations, we obtain well-converged work functions for Al, Pd, Au and Pt of (100), (110) and (111) surface orientations. For all the metals considered, the ordering of our calculated work functions of the three surface orientations agrees with experiment. Our findings reveal the importance of the FFT grid commensurability issue, which is usually neglected in practice, in obtaining accurate metal work functions, and are also meaningful to other DFT calculations which can be affected by the FFT grid commensurability issue.

Keywords: work function, plane-wave density-functional theory, DFT, fast Fourier transform, FFT.

1. Introduction

The work function of a metal is defined as the minimum energy needed to remove an electron from the metal interior to an infinite distance from the metal surface[1]. It is a fundamental surface property of a metal and is important to many surface-related phenomena such as charge injection at interfaces and surface corrosion. Experimentally, it is usually measured by photoemission methods such as X-ray photoelectron spectroscopy (XPS)[2]. Computationally, it can be calculated within the framework of first-principles density functional theory (DFT) by simulating a supercell containing a metal slab. The work function is given by the difference between the electrostatic potential energy in the vacuum region of the supercell and the Fermi energy of the metal slab. With this method, work functions of 19 common bcc and fcc metals of six close-packed surfaces have been predicted[3]. Fall *et al.*[1], however, showed that such slab supercell calculations can suffer significant quantum size effects, with poor convergence of the Fermi energy (and hence the work function) as a function of slab thickness. To reduce these finite-size effects and improve convergence, they introduced what is known as the 'bulk reference' method in which the Fermi energy of the metal slab is determined by referencing it to the relative position of the Fermi energy and the average electrostatic potential calculated for bulk metal. Under the 'bulk reference' method, they obtained work functions for aluminum of (100), (110) and (111) surfaces with the numerical uncertainty to be around 0.03 eV[4]. Chen *et al.*[5] obtained work functions within 5% of the experimental data for the (111) surface of Al, Ag, Au, Pd and Pt with a nine-layer metal slab. Singh-Miller *et al.*[6] found a quick convergence (by 7 layers) of the work function of the unrelaxed Pd(100) slab.

Despite this progress in improving the accuracy and size convergence of work function calculations using first-principles DFT, values reported in the literature for the calculated work functions of nominally the same metal surface have surprising variation. Table 1.1 summarizes the work functions of Al (100), (110) and (111) surfaces reported in the literature, calculated within the plane-wave pseudopotential (PWPP) DFT approach. Experimentally-determined values are provided in the bottom row for comparison. It is tempting to attribute these differences to the use of different pseudopotentials, exchange and correlation functionals and basis sets; however, there are discrepancies even among reports that use very similar methods and approximations. For example, the difference of the calculated work function in reference 4 and 7 is 0.55 eV, which is quite big considering that the variation in work functions of three surfaces is only within 0.17 eV according to the experimental fact. This is somewhat unsatisfactory for such a fundamental electronic property. These differences indicate there may be other computational and/or numerical factors that affect work function calculations and that have not been sufficiently controlled.

In the 'bulk reference' method, a key parameter to be determined is the electrostatic potential. In DFT calculations, it is sampled on a fast Fourier transform (FFT) grid. For a certain metal slab supercell, different choices of the FFT sampling patterns, i.e.,

Table 1.1: A summary of work functions of Al surfaces from the literature, calculated within the plane-wave pseudopotential DFT formalism with different approximations for exchange and correlation (XC), namely the local-density approximation (LDA) and generalised-gradient approximation (GGA), and different types of psuedopotential. The bottom row gives experimental results for comparison.

XC	Pseudopotential	Al(111) (eV)	Al(100) (eV)	Al(110) (eV)
GGA	Norm-conserving	4.02[6]	4.30[6]	4.09[6]
GGA	Ultrasoft	4.17[8], 4.09[9]		
GGA	PAW	4.20[10], 4.08[11]	4.27[10], 4.32[12]	3.96[10], 3.92[13]
LDA	Norm-conserving	4.25[4], 3.7[7]		4.30[4], 4.12[14], 4.32[15]
LDA	Ultrasoft	4.16[16]		
LDA	PAW	4.36[10]	4.41[10]	4.08[10]
	Experiment	4.24 ± 0.02[17]	4.41 ± 0.03[17]	4.28 ± 0.02[17]

whether or not the chosen FFT grid is commensurate with the underlying atomic structure, can give different values of the electrostatic potential in the middle of the metal slab, which determines the final calculated work function. In other words, the choice of the FFT grid results in some uncertainty in the calculated work function of a certain metal surface. We suspect that different choices of the FFT grid can explain the variation in calculated work functions of the same metal surface to some extent.

In this paper, we show that for PWPP DFT calculations of work functions using the bulk reference method, the commensurability of the FFT grid with atomic planes of a metal slab supercell has a significant influence on the convergence and precision of DFT calculations of work functions. We show that choosing the FFT grid to be commensurate with the atomic planes leads to significantly better convergence with respect to several parameters including basis set size, slab thickness, and the length of the vacuum region in the slab supercell, and therefore accurate values of work function can be obtained. On the other hand, incommensurate FFT grid can lead to poor convergence and inaccurate work function values. With the commensurability of FFT grid with atomic position controlled, we obtain well-converged and accurate work functions for Al, Pd, Au and Pt, which all have a fcc crystal structure and can be used as electrode materials[5,18]. For all metals studied, the surface orientations we consider are (100), (110) and (111), which are the most commonly occurring and most frequently studied surface planes of fcc metals. The knowledge gained from this limited selection of metal surfaces greatly advances our understanding of work-function calculations within the bulk reference method and goes a long way towards studying other metal surfaces. Whilst the numerical imprecision caused by incommensurate FFT grid can be mitigated to some extent by interpolating the electrostatic potential obtained from a DFT calculation onto a very fine grid, because the commensurability of the FFT grid with the atomic structure is not something that

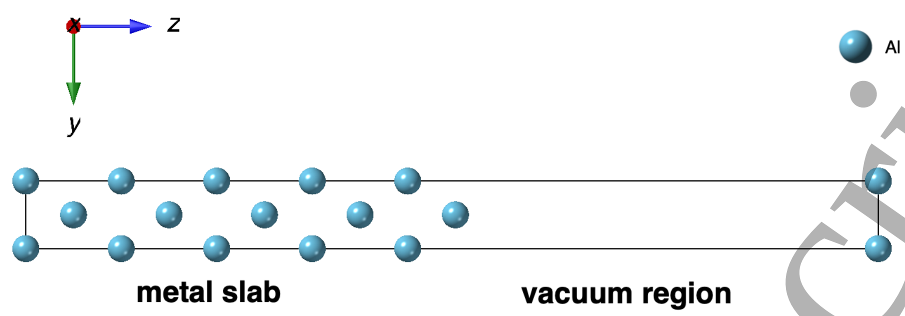

Figure 2.1: An illustration of a periodic metal slab supercell containing ten metal layers and a vacuum region used in DFT calculations of work function.

users of plane-wave DFT codes typically control or consider in detail, we believe that this is a potential source of the scatter in calculated work functions in the literature, and should be paid attention to for accurate work function calculations.

2. Methods

2.1. The bulk reference method

When calculating metal work function within the framework of DFT, a supercell containing a metal slab and a vacuum region, as shown in Fig. 2.1, is usually needed. To illustrate the bulk reference method, we plot the planar and macroscopic electrostatic potential calculated along the z-axis for such a metal slab supercell, and the alignment of electrostatic potential of the metal slab with that of a bulk metal in Fig. 2.2.

Within the bulk reference method[1], and with reference to the schematic slab (periodic) supercell setup shown in Fig. 2.1, the work function ϕ is calculated as

$$\phi = \widehat{V}^{\mathrm{slab}}_{\mathrm{vac}} - (\widehat{V}^{\mathrm{slab}}_{\mathrm{metal}} + E^{\mathrm{bulk}}_{\mathrm{F}} - \widehat{V}^{\mathrm{bulk}}), \tag{1}$$

where $\widehat{V}^{\mathrm{slab}}_{\mathrm{vac}}$ is the so-called "macroscopic average" local electrostatic potential in the middle of the vacuum region of the slab supercell, $\widehat{V}^{\mathrm{slab}}_{\mathrm{metal}}$ is the same quantity evaluated in the middle of the metal slab, and $\widehat{V}^{\mathrm{bulk}}$ and $E^{\mathrm{bulk}}_{\mathrm{F}}$ are the macroscopic average local electrostatic potential and Fermi energy of the bulk metal (obtained from a separate bulk calculation), respectively. The term in parenthesis in Equation (1) represents the Fermi energy of the metal slab $E^{\mathrm{slab}}_{\mathrm{F}}$, which is effectively calculated by referencing it to the macroscopic average potential in the bulk-like region in the deepest part of the metal slab ($\widehat{V}^{\mathrm{slab}}_{\mathrm{metal}}$) using the relative positions of the same quantities for the bulk metal ($E^{\mathrm{bulk}}_{\mathrm{F}}$ and $\widehat{V}^{\mathrm{bulk}}$), as illustrated in Fig. 2.2.

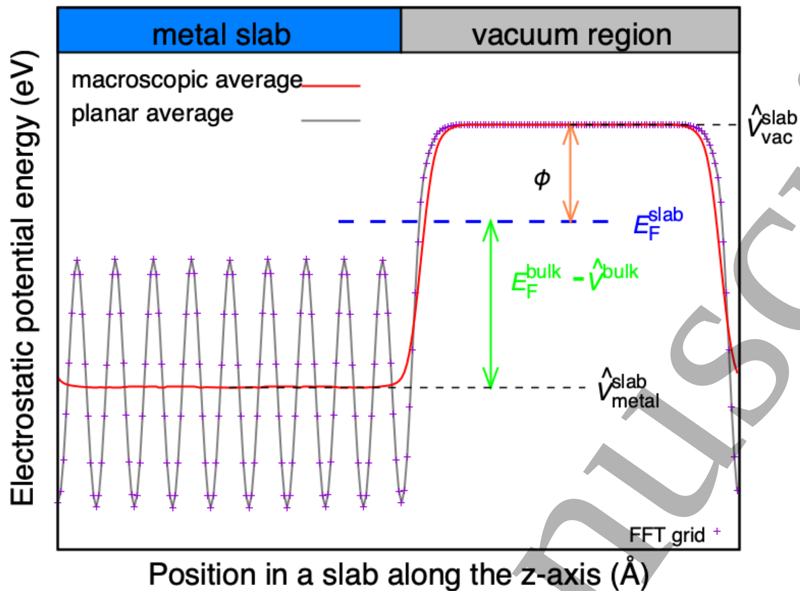

Figure 2.2: An illustration of the 'bulk reference' method with a periodic slab supercell containing ten atomic layers (N_{metal}=10) and a vacuum region of 17.98 Å (L_{vac}=17.98 Å) along the z-direction. The planar averaged potential [Equation (2)] is shown with the grey line, and the macroscopic averaged potential [Equation (3)] is shown with the red line. In practice, the electrostatic potential is sampled on a discrete FFT grid (purple symbols). The Fermi energy of the slab E_F^{slab} is obtained by referencing its difference with the macroscopic averaged electrostatic potential in the middle of the metal slab $\widehat{V}^{\mathrm{slab}}_{\mathrm{metal}}$ to $E_F^{\mathrm{bulk}} - \widehat{V}^{\mathrm{bulk}}$ (shown in green) obtained from a separate calculation on bulk metal [Equation (1)].

The macroscopic average local potential is calculated from the local electrostatic potential $V(\mathbf{r})$ that can be obtained from a DFT calculation. $V(\mathbf{r})$ is the sum of the local part of the ionic pseudopotential and the Hartree potential and is usually available on a grid of points in the computational cell that is the same as the FFT grid associated with the electronic charge density. $\widehat{V}(z)$ is obtained by first computing the planar average local electrostatic potential,

$$\overline{V}(z) = \frac{1}{S}\int_S V(\mathbf{r})\,\mathrm{d}S, \tag{2}$$

where S is the surface spanned by the slab in the (periodic) computational cell and we have assumed that the slab surface is perpendicular to the z-axis of the computational cell. This planar averaged potential is then smoothed by convolving with a filter function $f(z)$ to give the macroscopic average potential $\widehat{V}(z)$:

$$\widehat{V}(z) = \int f(z-z')\overline{V}(z')\,\mathrm{d}z'. \tag{3}$$

Different smoothing/filter functions are possible[19] and, in this work, we use a rectangle function of width equal to the interplanar distance d in the centre of the metal slab, and a height $1/d$, to give

$$\widehat{V}(z) = \frac{1}{d}\int_{-d/2}^{+d/2} \overline{V}(z - z')\,\mathrm{d}z'. \tag{4}$$

The process of macroscopic averaging smooths out the large spatial oscillations in the electrostatic potential caused by the discreteness of the atomic positions[19]. For a bulk calculation, $\widehat{V}(z)$ is a constant that is precisely equal to the direct average of the local electrostatic potential over the computational cell, $\frac{1}{V_{\mathrm{cell}}}\int_{V_{\mathrm{cell}}} V(\mathbf{r})\,\mathrm{d}^3r$. For a slab calculation, $\widehat{V}(z)$ will, in general, have some spatial variation and, for the purpose of evaluating the work function in Equation (1), $\widehat{V}_{\mathrm{vac}}^{\mathrm{slab}}$ and $\widehat{V}_{\mathrm{metal}}^{\mathrm{slab}}$ are taken at the middle of the vacuum and metal slab regions of the slab supercell, respectively, as illustrated in Fig. 2.2.

2.2. Calculation details

We calculate the work functions of the face-centred cubic (FCC) metals Al, Pt, Au and Pd for three of their surfaces, namely (100), (110) and (111). In each case, we use a primitive surface unit cell (i.e., there is only one inequivalent atom in each atomic plane of the slab). The initial interplanar spacings for the three different surfaces are $a_0/2$, $\sqrt{2}a_0/4$ and $\sqrt{3}a_0/3$, respectively, where a_0 is the equilibrium lattice constant of the FCC unit cell of the bulk metal. We allow the surfaces to relax whilst constraining three (four) atomic layers in the middle of the slab to be fixed to the bulk interplanar spacing when there is an odd (even) number of atomic layers in the slab. For each system, to ensure maximum consistency between the slab supercell calculations and bulk calculations that are used to compute the work function, we use a bulk unit cell taken from the middle (bulk-like) region of the slab supercell to calculate $\widehat{V}^{\mathrm{bulk}}$ and $E_{\mathrm{F}}^{\mathrm{bulk}}$ in Equation (1).

DFT calculations were carried out using the PWscf code of the Quantum-ESPRESSO software package[20]. In all cases, the Perdew-Burke-Ernzerhof (PBE) functional[21] was used to describe exchange and correlation. Rappe-Rabe-Kaxiras-Joannopoulos (RRKJ) ultrasoft pseudopotentials[22] were used for Pd, Au and Pt, and an RRKJ norm-conserving pseudopotential[22] was used for Al. Unless otherwise stated, for Al, Pd, Au and Pt, the plane-wave kinetic energy cutoffs were, respectively, 32 Ry, 48 Ry, 48 Ry and 40 Ry for wavefunctions and 128 Ry, 288 Ry, 192 Ry and 160 Ry for the charge density. Marzari-Vanderbilt smearing was used in all calculations with a smearing width of 0.01 Ry. In calculations on slab supercells, a $16 \times 16 \times 1$ Monkhorst-Pack k-point mesh[23] was used to sample the first Brillouin zone. In calculations on bulk metal, an $8 \times 8 \times 8$ k-point mesh was used for primitive FCC unit cells used to calculate equilibrium lattice parameters, and a $36 \times 36 \times 26$ mesh was used for the unit cells used to obtain $\widehat{V}^{\mathrm{bulk}}$ and $E_{\mathrm{F}}^{\mathrm{bulk}}$. For the surface relaxations, the force and the total energy thresholds were 0.026 eV/Å and 1.4 meV, respectively. The calculated bulk lattice constants of the four metals are shown in Table 2.1; experimental values are also provided for comparison.

Table 2.1: Bulk lattice constants a_0 calculated with DFT (this work) and from experiment[24]. $\Delta = (a_0^{\mathrm{DFT}} - a_0^{\mathrm{expt}})/a_0^{\mathrm{expt}}$ is the fractional difference between the calculated and experimental values.

	a_0^{DFT} (Å)	a_0^{expt}(Å)	Δ (%)
Al	4.06	4.05	0.24
Pd	3.96	3.89	1.80
Au	4.17	4.08	2.21
Pt	3.99	3.92	1.79

3. Results and discussion

3.1. Convergence

When calculating metal work functions within the bulk reference method, the first thing that may occur to us is the convergence of work functions. Here, we consider the convergence of the work function with respect to basis set size, the length of the vacuum region in the slab supercell (L_{vac}) and the number of metal layers in the slab (N_{metal}), which are commonly checked in DFT calculations. Usually, it is believed that the work function of a metal surface can converge well as long as these parameters are large enough. However, in the following paragraph, we will show how work function shows significant non-monotonic convergence with respect to these parameters.

In PWPP DFT codes, the local electrostatic potential, which enters the calculation of the work function through Equation (1), is typically represented on the same FFT grid that is used for the electronic charge density. This FFT grid depends on the chosen kinetic energy cutoff for the charge density, and hence the size of the plane-wave basis used in the calculation. Figure 3.1(a) shows the convergence of the work function with basis-set size for a 10-layer Al(100) slab with $L_{\mathrm{vac}} = 18.27$ Å, where our measure of basis-set size is the number n_{zFFT} of FFT grid spacings along the perpendicular direction between two interatomic planes in the interior (bulk-like) region of the metal slab. We see immediately that the work function varies very non-systematically (green data) except when the FFT grid is chosen to be perfectly commensurate with the interlayer spacing, in other words, when n_{zFFT} is an integer (purple data). For the commensurate case, the variation in the work function is at most 1 meV from $n_{\mathrm{zFFT}} = 12$ to $n_{\mathrm{zFFT}} = 27$, whereas for the incommensurate case it varies by almost 200 meV over the same range of n_{zFFT} and shows no indication of systematic convergence even at the largest incommensurate value of $n_{\mathrm{zFFT}} = 26.67$ that we went up to, which corresponds to a plane-wave energy cutoff for the charge density of 470 Ry. It is important to note that commensurability of the FFT grid with the interplanar spacing is not typically guaranteed in a PWPP DFT calculation unless the size of the FFT grid is explicitly specified to be such in the input file.

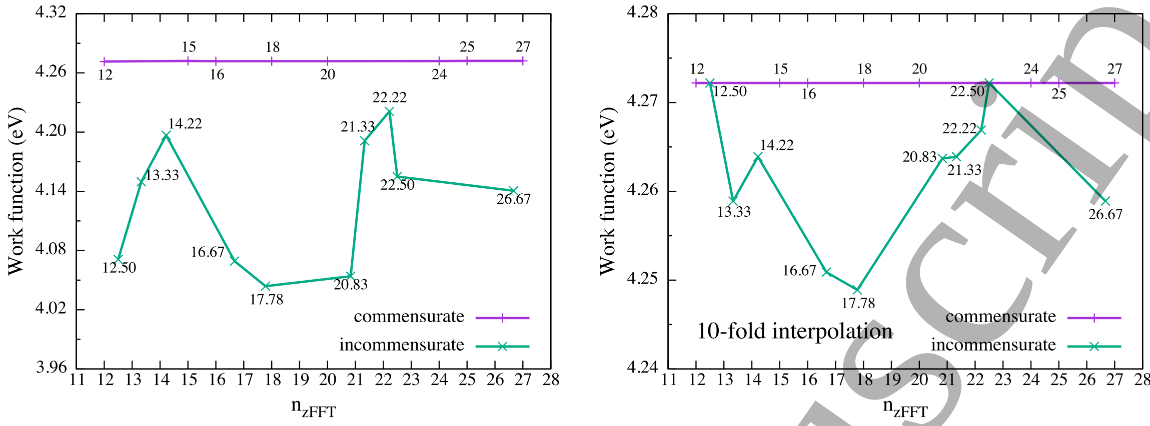

(a) (b)

Figure 3.1: The work function of a 10-layer Al(100) slab as a function of the number n_{zFFT} of FFT grid spacings between two adjacent interatomic planes in the interior (bulk-like) region of the slab. Panel (a): comparison between the FFT grid being commensurate (purple) and incommensurate (green) with the interlayer spacing in the interior (bulk-like) region of the metal slab. Panel (b): the same as panel (a) but with a 10-fold interpolation applied to the local potential $\overline{V}(z)$. The number adjacent to each data point shows the value of n_{zFFT} for each calculation.

Next, we consider convergence with respect to L_{vac}. Figure 3.2(a) shows the work function of a 10-layer Al(100) slab with respect to L_{vac}. It can be seen that in the incommensurate case (green data), the work function shows no systematic convergence and varies by up to 0.32 eV even when $L_{\mathrm{vac}} \geq 15$ Å, whereas in the commensurate case (purple data), there is rapid convergence within 1 meV by $L_{\mathrm{vac}} = 10.73$ Å.

We also study the convergence of the work function of a Al(100) slab with respect to N_{metal}. In Figure 3.3(a), for the incommensurate case (green data), the work function shows no systematic convergence and shows a variation of 0.64 eV even when N_{metal} is over 15. In contrast, for the commensurate case (purple data), the convergence is within 35 meV by $N_{\mathrm{metal}} = 9$.

With respect to n_{zFFT}, L_{vac} and N_{metal}, the work function does not show any trend of convergence for the incommensurate case without interpolation, and a 10-fold interpolation greatly improves the convergence (Figure 3.1(b), Figure 3.2(b) and Figure 3.3(b)). By contrast, at integer n_{zFFT}, the work function is stable and is almost not influenced by interpolation, which can be easily observed in Figure 3.1. It seems that the convergence of work function is more about whether or not n_{zFFT} is an integer, i.e., whether or not the FFT grid is commensurate with the positions of underlying metal planes. According to Equation (1), $E_{\mathrm{F}}^{\mathrm{bulk}}$ and $\widehat{V}^{\mathrm{bulk}}$ are from bulk metal calculations and are constant in different slab supercell calculations. Therefore, the commensurability of FFT grid actually influences the convergence of work function through the values of

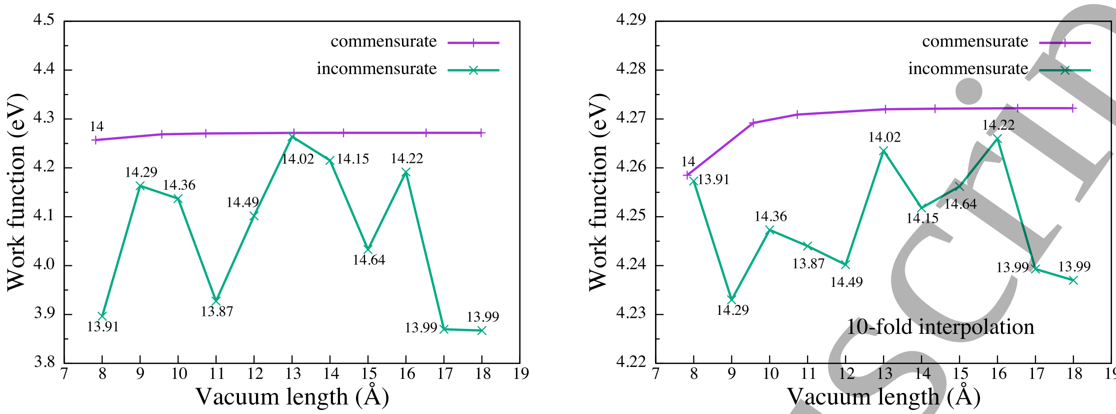

(a) (b)

Figure 3.2: The work function of a 10-layer Al(100) slab as a function of the length L_{vac} of the vacuum region separating periodic images in the supercell. Panel (a): comparison between the FFT grid being commensurate (purple) and incommensurate (green) with the interlayer spacing in the interior (bulk-like) region of the metal slab. Panel (b): the same as panel (a) but with a 10-fold interpolation applied to the local potential $\overline{V}(z)$. The number next to each data point shows the corresponding n_{zFFT}; for the case in which the FFT grid is commensurate (purple data), $n_{\mathrm{zFFT}} = 14$ for all data points.

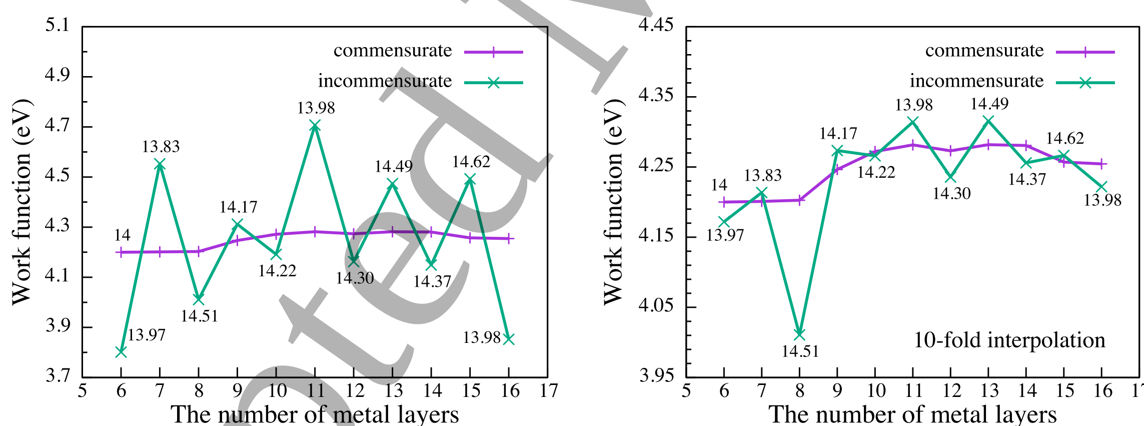

(a) (b)

Figure 3.3: The work function of a Al(100) slab as a function of N_{metal}. Panel (a): comparison between the FFT grid being commensurate (purple) and incommensurate (green) with the interlayer spacing in the interior (bulk-like) region of the metal slab. Panel (b): the same as panel (a) but with a 10-fold interpolation applied to the local potential $\overline{V}(z)$. The number next to each data point shows the corresponding n_{zFFT}; for the case in which the FFT grid is commensurate (purple data), $n_{\mathrm{zFFT}} = 14$ for all data points.

$\widehat{V}_{\text{vac}}^{\text{slab}}$ and $\widehat{V}_{\text{metal}}^{\text{slab}}$. We have checked that the value of $\widehat{V}_{\text{vac}}^{\text{slab}}$ is not affected by the FFT grid commensurability issue, while $\widehat{V}_{\text{metal}}^{\text{slab}}$ shows great dependence on it, which will be explained in detail in the next section.

3.2. The FFT grid commensurability issue

To study the effects of n_{zFFT} on $\widehat{V}_{\text{metal}}^{\text{slab}}$, we performed two 10-layer Al(100) slab calculations under same conditions except that for one case (commensurate), n_{zFFT} is set to be an integer (15), while for the other one (incommensurate), n_{zFFT} is a non-integer (17.8). In Figure 3.4, we show $\overline{V}(z)$ (planar average potential) within the middle four atomic planes (denoted by dashed lines) of the slab of the commensurate and the incommensurate cases in the top and middle panels, respectively. Compared to the commensurate case, the sampling pattern of $\overline{V}(z)$ between two atomic planes is not guaranteed to be the same for the incommensurate case. In the bottom panel of Figure 3.4, we show the resulting $\widehat{V}(z)$ (macroscopic average potential) for the two cases. The $\widehat{V}(z)$ of the commensurate case shows a much smaller oscillation, with the oscillation magnitude $\Delta\widehat{V}$ (defined as the difference between the maximum and the minimum of $\widehat{V}$ within the middle two atomic planes) to be only 15 meV, compared to 490 meV of the incommensurate case. Furthermore, $\widehat{V}$ at the central point of the metal slab, i.e., $\widehat{V}_{\text{metal}}^{\text{slab}}$ in Equation (1), shows a difference of 0.24 eV between the two cases.

To further compare $\widehat{V}(z)$ calculated with commensurate and incommensurate FFT grids, we study the change of $\widehat{V}(z)$ within the middle two atomic planes of a 10-layer Al(100) slab calculation with different n_{zFFT}. In Figure 3.1, we have shown the convergence of work function with respect to n_{zFFT}. $\widehat{V}(z)$ within the middle two atomic planes is characterised by the middle point potential, which is used as $\widehat{V}_{\text{metal}}^{\text{slab}}$ in Equation (1), and the oscillation magnitude $\Delta\widehat{V}$ defined before. In Figure 3.5(a), we show that for the commensurate cases (purple), both the middle point potential and $\Delta\widehat{V}$ remain stable with the increase of n_{zFFT}, while for the incommensurate cases (green), the two parameters show significant non-monotonicity of convergence, which explains the poor convergence of work function of incommensurate cases in Figure 3.1(a).

3.3. A further averaging process

In principle, $\widehat{V}(z)$ should be flat in the middle 'bulk-like' region of a metal slab. However, in Figure 3.4 (bottom), it is shown that even if the FFT grid commensurability issue is controlled (purple), $\widehat{V}(z)$ still shows a small variation (15 meV) in the middle region of a metal slab. In Section 2.1, we mention that $\widehat{V}_{\text{metal}}^{\text{slab}}$ in Equation (1) is taken at the middle of a metal slab region. In fact, the variation shown in Figure 3.4 (bottom) suggests that there is some uncertainty in choosing the particular z-axis FFT grid point in the middle region to obtain $\widehat{V}_{\text{metal}}^{\text{slab}}$.

To eliminate the variation, we performed a further averaging process over $\widehat{V}(z)$ in the middle region and show its effects on the convergence of work function with respect to N_{metal}. For an odd and an even number of atomic layers in a metal slab, we averaged

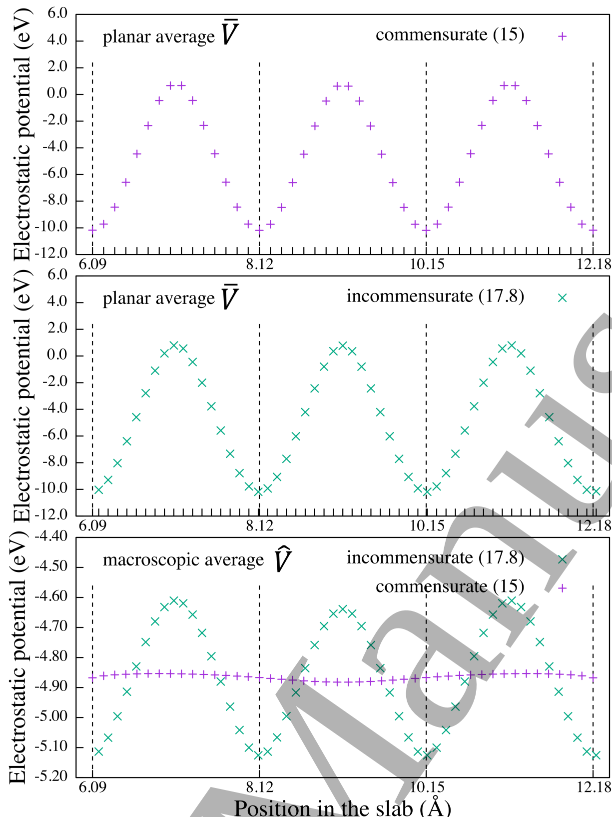

Figure 3.4: Planar average potential $\overline{V}(z)$ (top and middle) and macroscopic average potential $\widehat{V}(z)$ (bottom) within the middle four atomic planes of commensurate and incommensurate 10-layer Al(100) slab calculations. The positions of atomic planes are shown with dashed lines.

$\widehat{V}(z)$ within the middle three and middle two atomic layers, respectively, and the further averaged macroscopic average potential was used as $\widehat{V}^{\text{slab}}_{\text{metal}}$ in Equation (1). In Figure 3.6(a), it is shown that the work function can converge to within 30 meV by 11-layers for both commensurate and incommensurate cases. Also, the difference of work function calculated at a certain N_{metal} between commensurate and incommensurate FFT grids has a maximum value of 6 meV.

Compared to Figure 3.3(a), it can be seen that the further averaging process has almost no effect on the convergence of work function calculated with commensurate FFT grids, but it can greatly improve the convergence of incommensurate FFT grids. To the best of our knowledge, this further averaging process is not routinely performed in these sorts of calculations. The fact that $\widehat{V}(z)$ in the middle atomic region is not perfectly flat is just an indication that the centre of the slab is not quite at the 'bulk-like' limit. Nevertheless, the further averaging process does seem to alleviate the poor convergence of work functions calculated with incommensurate FFT grids.

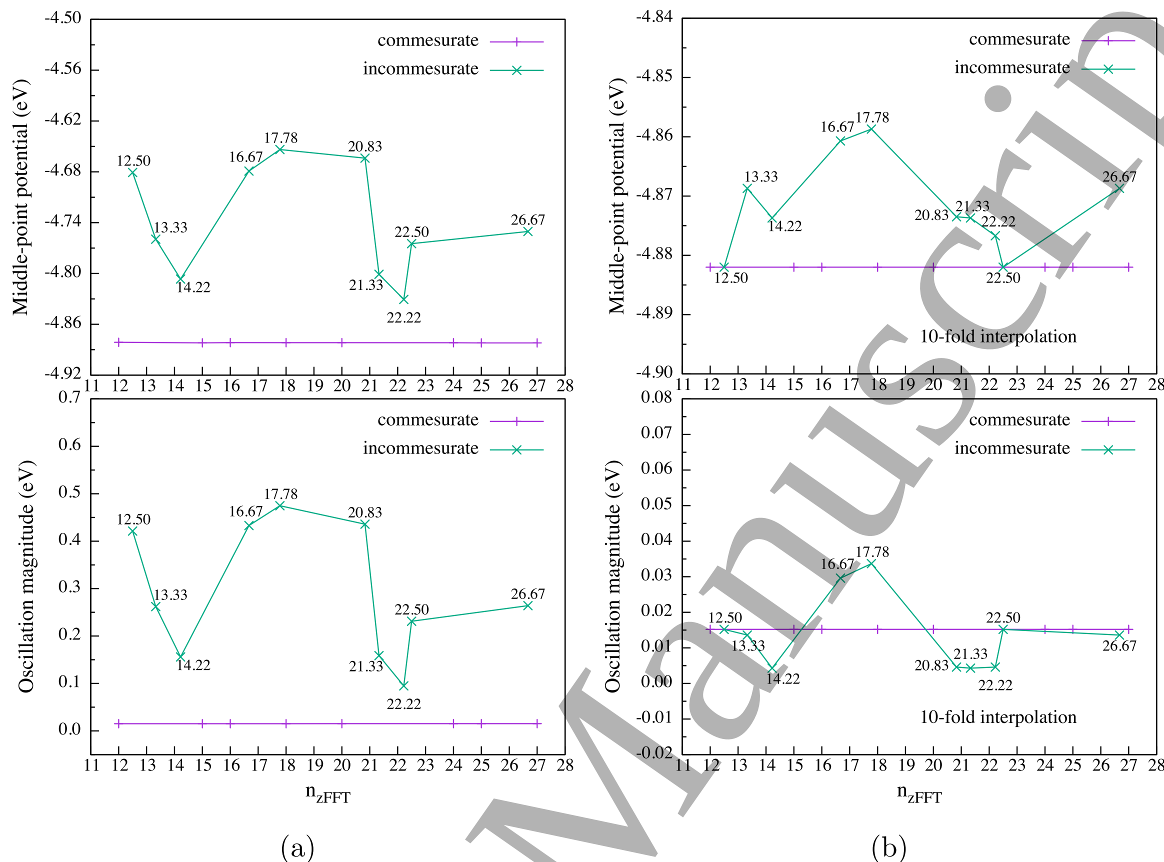

Figure 3.5: The middle-point potential (top) and oscillation magnitude (bottom) of $\widehat{V}(z)$ within middle two atomic planes of a 10-layer Al(100) slab as a function of n_{zFFT}. Panel (a): comparison between the FFT grid being commensurate (purple) and incommensurate (green) with the interlayer spacing in the interior (bulk-like) region of the metal slab. Panel (b): the same as panel (a) but with a 10-fold interpolation applied to the local potential $\overline{V}(z)$. The number adjacent to each data point shows the value of n_{zFFT} for each calculation.

3.4. Work functions of Al, Pd, Au and Pt

We now show the convergence of work function with respect to N_{metal} with the FFT grid commensurability controlled for Al, Pd, Au and Pt of the (100), (110) and (111) surface orientations in Figure 3.7. For a certain metal surface, we performed all slab supercell calculations with n_{zFFT} controlled to be a constant integer. The vacuum lengths in different calculations may vary and are all above 15 Å. $\widehat{V}^{\mathrm{slab}}_{\mathrm{metal}}$ in Equation (1) is still taken at the middle of a metal slab region. We have checked that with the FFT grid commensurability controlled, a 10-fold interpolation applied to $\overline{V}(z)$ has almost no effect on the calculated work function. Therefore, we only show the data without interpolation here.

For each metal surface, we show the work function value for the largest slab thickness considered as the number before a slash in the left part of Table 3.1. The

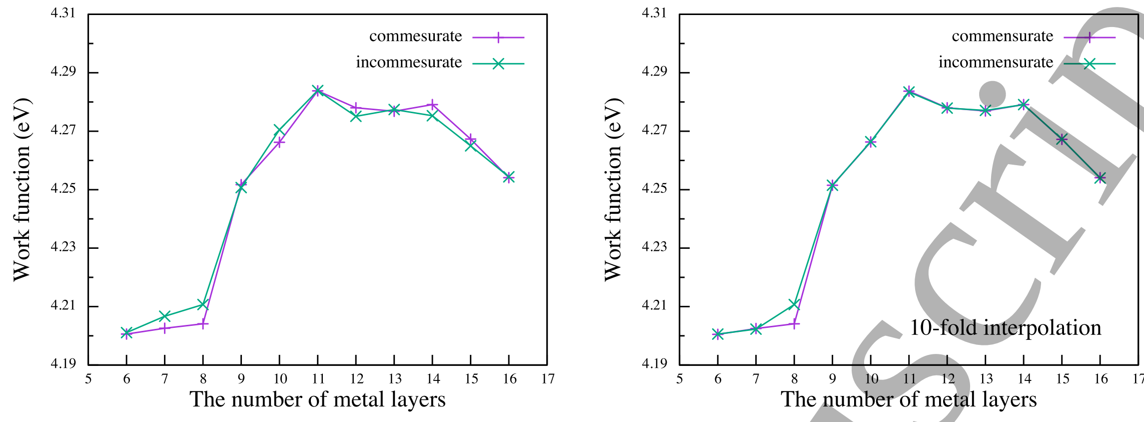

(a) (b)

Figure 3.6: The work function of a Al(100) slab as a function of N_{metal} after a further averaging process is performed. Panel (a): comparison between the FFT grid being commensurate (purple) and incommensurate (green) with the interlayer spacing in the interior (bulk-like) region of the metal slab. Panel (b): the same as panel (a) but with a 10-fold interpolation applied to the local potential $\overline{V}(z)$.

experimental values are given in the right part of the table for comparison. For all metals studied, the ordering of the calculated work function of the three surface orientations is the same with the experimental fact: for Pd, Au and Pt, it is $\psi_{111} > \psi_{100} > \psi_{110}$, showing that ψ increases as the atomic packing density of the surface increases; for Al, it is $\psi_{100} > \psi_{110} > \psi_{111}$. The anomaly of Al has also been observed in other DFT calculations within the plane-wave pseudopotential framework[4,6] of the work functions of Al surfaces. However, we also notice that there do exist discrepancies in values between our calculations and experimental data. The experimentally measured work functions are all higher than our calculated values, and the maximum difference is of 0.65 eV for the Pd(111) surface. The discrepancy may result from surface reconstruction of metals in experiment that we don't consider in our calculations. Also, in our study, we only use PBE as the exchange and correlation functional, and other functionals such as LDA may give results closer to the experimental values.

To show the effect of the controlled FFT grid commensurability on the calculated work function, we also provide the value calculated without controlling the FFT grid commensurability, as the number after a slash in the left part of Table 3.1. The work functions calculated with commensurate and incommensurate FFT grids can have great discrepancies (e.g. 0.4 eV for Al(100) surface and 0.15 eV for Pd (111) surface), although small discrepancy (0.01 eV for Pt(110) surface) can also be seen. Furthermore, with incommensurate FFT grids, the ordering of calculated ϕ among (100), (110) and (111) orientations differs from the experiment fact for Al, Au and Pt. For example, the calculated ψ of the Al(100) surface is the smallest, while in experiment, the Al(100) surface has the largest work function. The above discussion suggests that in practice,

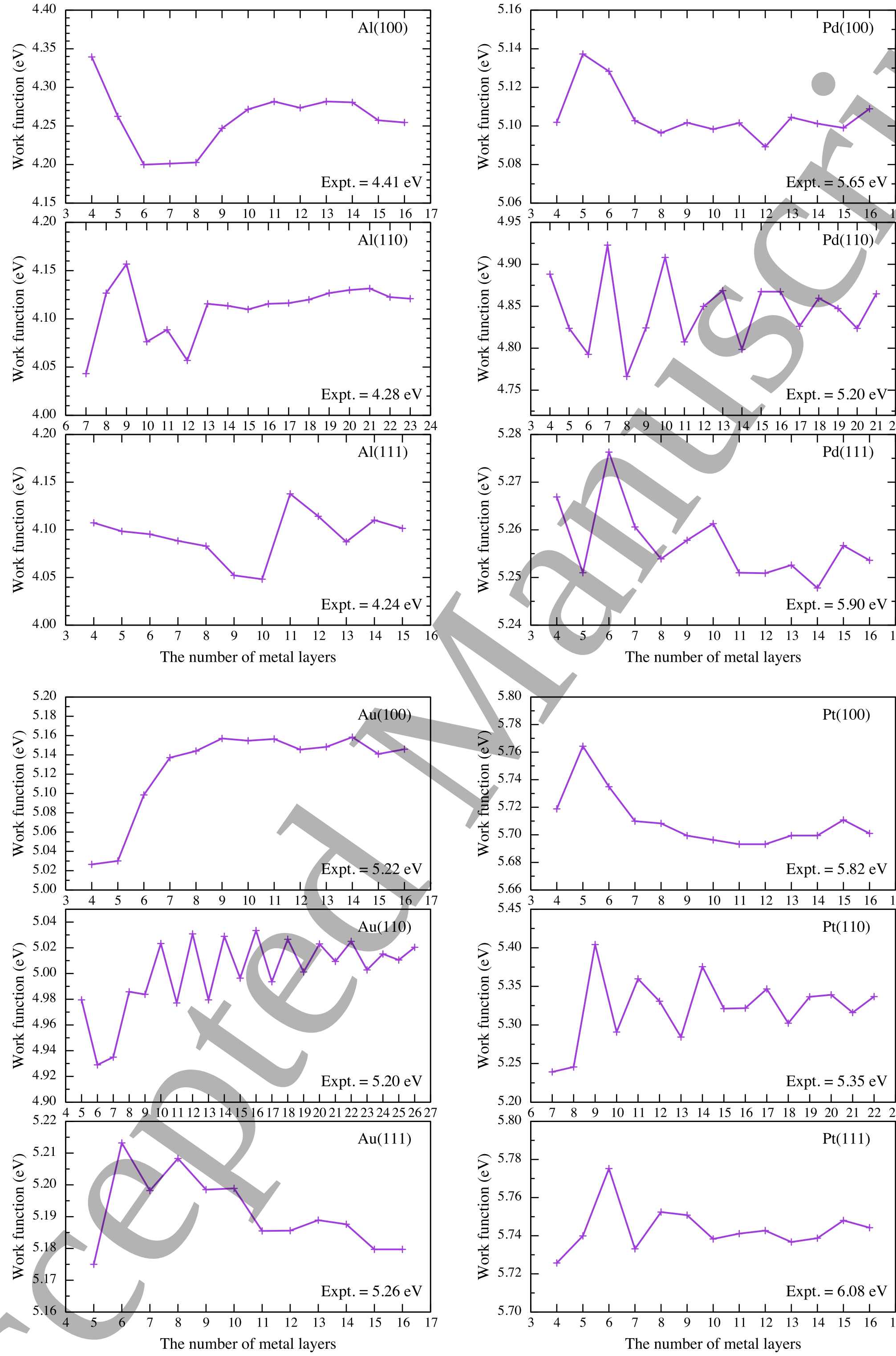

Figure 3.7: The convergence of calculated work function (with commensurate FFT grids) with respect to N_{metal} for (100), (110) and (111) surface orientations of Al, Pd, Au and Pt. In each subfigure, the experimental data is shown as a label in the right bottom corner for comparison.

Table 3.1: Calculated (left part) and experimental (right part) work functions of (100), (110) and (111) surface orientations of Al, Pd, Au and Pt. For calculated results, the work functions calculated with and without commensurate FFT grids are shown before and after a slash, respectively. For each metal surface, the value is for the largest slab thickness considered.

	Calculated results (eV)			Experimental results (eV)		
Surface	(111)	(100)	(110)	(111)	(100)	(110)
Al	4.10/4.18	4.25/3.85	4.12/4.18	4.24 ± 0.02[17]	4.41 ± 0.03[17]	4.28 ± 0.02[17]
Pd	5.25/5.10	5.11/4.93	4.86/4.88	5.90 ± 0.01[25]	5.65 ± 0.01[25]	5.20 ± 0.01[25]
Au	5.18/5.12	5.15/5.13	5.02/5.05	5.26 ± 0.04[26]	5.22 ± 0.04[26]	5.20 ± 0.04[26]
Pt	5.74/5.72	5.70/5.75	5.34/5.35	6.08 ± 0.15[27]	5.82 ± 0.15[27]	5.35 ± 0.05[28]

if we don't pay attention to the FFT grid commensurability issue, the calculated work functions may not only be quantitatively incorrect but also qualitatively.

4. Summary

In this paper, we have studied how the commensurability of FFT grid on which the electrostatic potential is evaluated with the atomic plane position of a metal slab influences the convergence and precision of metal work function calculated with the 'bulk reference' method. We find that without explicitly controlling the FFT grid commensurability issue, the work function of the Al(100) surface shows non-monotonic and poor convergence with respect to the basis set size n_{zFFT}, the amount of vacuum region in the supercell L_{vac}, and the number of metal layers in the slab N_{metal}. By contrast, commensurate FFT grid can lead to good convergence and accurate work function values. We have also shown that compared to incommensurate FFT grid, commensurate FFT grid gives rise to more stable and accurate macroscopic average potentials in the middle of a metal slab, which explains the improved convergence and precision of work function. Although we find that by applying a 10-fold interpolation to planar average electrostatic potential or doing a further average of macroscopic average electrostatic potential can alleviate the poor convergence with the incommensurate FFT grid, we believe that we can always obtain well-converged and accurate work functions by making the FFT grid commensurate with the underlying atomic position.

With the FFT grid commensurability issue controlled in each slab supercell calculation, we show good convergence of calculated work function of (100), (110) and (111) surface orientations for Al, Pd, Au and Pt. Also, for all metals studied, we obtain the same ordering of the calculated work functions among (100), (110) and (111) orientations to the experimental fact. For comparison, we show that without controlling the FFT grid commensurability issue, the obtained ordering is different with experiment, suggesting the importance of the FFT grid commensurability issue. Although there is discrepancy between our calculated work function values and experimental data, we believe that it may result from metal surface reconstruction in experiments and the choice of exchange and correlation functionals. Furthermore, the FFT grid commensurability issue is not limited to the four metals considered in this work, since the 'bulk reference' method is also applicable to metals with other crystal structures, i.e, body-centered cubic and hexagonal close packing, and surfaces of higher indexes.

Our conclusion is that to obtain well-converged and accurate metal work function in PWPP DFT calculations, we should always make the positions of atomic planes along the z-axis (perpendicular to surface) commensurate with the underlying FFT grid points along the z-axis. The FFT grid commensurability issue also exists in work function calculations within the bulk reference method for metals with other crystal symmetries and other surface orientations. Besides, it can be seen in DFT calculations of other material properties, such as the electron affinity defined as the energy difference between the vacuum level and the conduction band minimum of an insulator, that can be obtained with a surface slab supercell under the bulk reference method. Generally, it is important in DFT calculations where the properties of interest are sampled on a FFT grid, and we suggest that in these calculations, the sensitivity of the properties of interest to the FFT grid commensurability issue should always be checked to improve the precision of the calculations.

Acknowledgments

This work was supported by Hitachi Energy Research (earlier Hitachi ABB Power Grids Research), the China Scholarship Council, and the Centre for Doctoral Training in Theory and Simulation of Materials at Imperial College London (EPSRC grant EP/L015579/1). We also acknowledge support from the Thomas Young Centre under grant number TYC-101.

5. References

[1] C. Fall, N. Binggeli, and A. Baldereschi, "Deriving accurate work functions from thin-slab calculations," *Journal of Physics: Condensed Matter*, vol. 11, no. 13, p. 2689, 1999.

[2] O. Klyushnikov, "Method to determine the work function using x-ray photoelectron spectroscopy," *Journal of structural chemistry*, vol. 39, no. 6, pp. 944–947, 1998.

[3] J. Wang and S.-Q. Wang, "Surface energy and work function of fcc and bcc crystals: Density functional study," *Surface science*, vol. 630, pp. 216–224, 2014.

[4] C. Fall, N. Binggeli, and A. Baldereschi, "Anomaly in the anisotropy of the aluminum work function," *Physical Review B*, vol. 58, no. 12, p. R7544, 1998.

[5] L. Chen, T. D. Huan, Y. C. Quintero, and R. Ramprasad, "Charge injection barriers at metal/polyethylene interfaces," *Journal of materials science*, vol. 51, no. 1, pp. 506–512, 2016.

[6] N. E. Singh-Miller and N. Marzari, "Surface energies, work functions, and surface relaxations of low-index metallic surfaces from first principles," *Physical Review B*, vol. 80, no. 23, p. 235407, 2009.

[7] I. P. Batra, S. Ciraci, G. Srivastava, J. Nelson, and C. Fong, "Dimensionality and size effects in simple metals," *Physical Review B*, vol. 34, no. 12, p. 8246, 1986.

[8] A. Kokalj, "On the hsab based estimate of charge transfer between adsorbates and metal surfaces," *Chemical Physics*, vol. 393, no. 1, pp. 1–12, 2012.

[9] A. Kiejna and B. I. Lundqvist, "First-principles study of surface and subsurface o structures at al (111)," *Physical Review B*, vol. 63, no. 8, p. 085405, 2001.

[10] A. Patra, J. E. Bates, J. Sun, and J. P. Perdew, "Properties of real metallic surfaces: Effects of density functional semilocality and van der waals nonlocality," *Proceedings of the National Academy of Sciences*, vol. 114, no. 44, pp. E9188–E9196, 2017.

[11] E.-G. Kim and J.-L. Brédas, "The nature of the aluminum–aluminum oxide interface: A nanoscale picture of the interfacial structure and energy-level alignment," *Organic Electronics*, vol. 14, no. 2, pp. 569–574, 2013.

[12] S. Prada, U. Martinez, and G. Pacchioni, "Work function changes induced by deposition of ultrathin dielectric films on metals: A theoretical analysis," *Physical Review B*, vol. 78, no. 23, p. 235423, 2008.

[13] S. Cheng, C. M. Tan, T. Deng, F. He, S. Zhang, and H. Su, "Investigation of work function and surface energy of aluminum: An ab-initio study," in *2013 IEEE 5th International Nanoelectronics Conference (INEC)*, pp. 473–475, IEEE, 2013.

[14] A. Kiejna, J. Peisert, and P. Scharoch, "Quantum-size effect in thin al (110) slabs," *Surface science*, vol. 432, no. 1-2, pp. 54–60, 1999.

[15] K. Ho and K. Bohnen, "Investigation of multilayer relaxation on al (110) with the use of self-consistent total-energy calculations," *Physical Review B*, vol. 32, no. 6, p. 3446, 1985.

[16] S. Kajita, T. Nakayama, and J. Yamauchi, "Density functional calculation of work function using charged slab systems," in *Journal of Physics: Conference Series*, vol. 29, p. 023, IOP Publishing, 2006.

[17] J. Grepstad, P. Gartland, and B. Slagsvold, "Anisotropic work function of clean and smooth low-index faces of aluminium," *Surface Science*, vol. 57, no. 1, pp. 348–362, 1976.

[18] Y. Wang, S. J. Laihonen, M. Unge, and A. A. Mostofi, "The effect of chemistry and thermal fluctuations on charge injection barriers at aluminum/polyolefin interfaces," *Journal of Applied Physics*, vol. 134, no. 12, 2023.

[19] J. Junquera, M. H. Cohen, and K. M. Rabe, "Nanoscale smoothing and the analysis of interfacial charge and dipolar densities," *Journal of Physics: Condensed Matter*, vol. 19, no. 21, p. 213203, 2007.

[20] P. Giannozzi, O. Andreussi, T. Brumme, O. Bunau, M. B. Nardelli, M. Calandra, R. Car, C. Cavazzoni, D. Ceresoli, M. Cococcioni, N. Colonna, I. Carnimeo, A. D. Corso, S. de Gironcoli, P. Delugas, R. A. D. Jr, A. Ferretti, A. Floris, G. Fratesi, G. Fugallo, R. Gebauer, U. Gerstmann, F. Giustino, T. Gorni, J. Jia, M. Kawamura, H.-Y. Ko, A. Kokalj, E. Küçükbenli, M. Lazzeri, M. Marsili, N. Marzari, F. Mauri, N. L. Nguyen, H.-V. Nguyen, A. O. de-la Roza, L. Paulatto, S. Poncé, D. Rocca, R. Sabatini, B. Santra, M. Schlipf, A. P. Seitsonen, A. Smogunov, I. Timrov, T. Thonhauser, P. Umari, N. Vast, X. Wu, and S. Baroni, "Advanced capabilities for materials modelling with quantum espresso," *Journal of Physics: Condensed Matter*, vol. 29, no. 46, p. 465901, 2017.

[21] J. P. Perdew, K. Burke, and M. Ernzerhof, "Generalized gradient approximation made simple," *Physical review letters*, vol. 77, no. 18, p. 3865, 1996.

[22] A. M. Rappe, K. M. Rabe, E. Kaxiras, and J. Joannopoulos, "Optimized pseudopotentials," *Physical Review B*, vol. 41, no. 2, p. 1227, 1990.

[23] H. J. Monkhorst and J. D. Pack, "Special points for brillouin-zone integrations," *Physical review B*, vol. 13, no. 12, p. 5188, 1976.

[24] C. Kittel, P. McEuen, and P. McEuen, *Introduction to solid state physics*, vol. 8. Wiley New York, 1996.

[25] J. Hulse, J. Küppers, K. Wandelt, and G. Ertl, "Uv-photoelectron spectroscopy from xenon

adsorbed on heterogeneous metal surfaces," *Applications of Surface Science*, vol. 6, no. 3-4, pp. 453–463, 1980.

[26] G. Hansson and S. Flodström, "Photoemission study of the bulk and surface electronic structure of single crystals of gold," *Physical Review B*, vol. 18, no. 4, p. 1572, 1978.

[27] M. Salmeron, S. Ferrer, M. Jazzar, and G. Somorjai, "Photoelectron-spectroscopy study of the electronic structure of au and ag overlayers on pt (100), pt (111), and pt (997) surfaces," *Physical Review B*, vol. 28, no. 12, p. 6758, 1983.

[28] R. Vanselow and X. Li, "The work function of kinked areas on clean, thermally rounded pt and rh crystallites: Its dependence on the structure of terraces and edges," *Surface science*, vol. 264, no. 1-2, pp. L200–L206, 1992.